RSC Advances

PAPER

View Article Online
View Journal | View Issue

Cite this: *RSC Adv.*, 2017, **7**, 31512

Electrochemical hydrogenated TiO_2 nanotube arrays decorated with 3D cotton-like porous MnO_2 enables superior supercapacitive performance†

Jiaqin Liu,*[acd] Juan Xu,[ab] Yan Wang,[ac] Jiewu Cui,[ac] Hark Hoe Tan[d] and Yucheng Wu*[ac]

Highly ordered TiO_2 nanotube arrays (TNTAs) have shown great promise to serve as an efficient current collector as well as an outstanding support for the application of constructing high performance supercapacitor electrode materials. In this study, a novel-structured MnO_2/EH-TNTAs electrode with superior supercapacitive performance was developed by galvanostatic electrodeposition of MnO_2 nanoflakes onto both the outer and inner walls of electrochemically hydrogenated TNTAs (EH-TNTAs). The as-fabricated MnO_2/EH-TNTAs electrode could achieve a specific capacitance of up to 650.0 F g^{-1} at 1.0 A g^{-1} with 86.9% of the initial capacitance remaining after 5000 charge/discharge cycles at 5 A g^{-1}, outperforming other reported TNTAs-based electrodes. The prominent supercapacitive performance of MnO_2/EH-TNTAs electrode could be attributed to the unique 3D cotton-like porous structure and high specific surface area of MnO_2 deposit as well as the remarkably improved electrical conductivity and electrochemical performances of EH-TNTAs induced by the introduction of oxygen vacancies during the electrochemical hydrogenation process. This work offers theoretical insight and practical guidelines for TNTAs-based electrodes applied for high-performance supercapacitors as well as other energy storage devices.

Received 1st May 2017
Accepted 13th June 2017

DOI: 10.1039/c7ra04883a

rsc.li/rsc-advances

Introduction

Supercapacitors (SCs), also called electrochemical capacitors, store energy using either reversible ion adsorption (electrical double layer capacitors, EDLCs) or fast surface redox reactions (pseudo-capacitors, PCs). They can fill the gap between batteries and conventional solid state and electrolytic capacitors due to their high power density, rapid charge/discharge rates and long cycling life. Compared to the EDLCs, whose capacitances are restricted by the limited charge accumulation in the electrical double layer, PCs achieved substantially much higher specific capacitances through surface redox reactions, and thus, have a potential to meet the requirements of future energy storage systems.[1–4] Electrode materials are the most critical component determining the performance and the cost of the SCs. For EDLCs, carbon-based materials are commonly used as electrodes due to their high electrical conductivity, long-term electrochemical stability and moderate cost, while for PCs, conducting polymers and transition metal oxides, hydroxides and sulfides are the two main categories of pseudo-capacitive active materials. Many kinds of conducting polymers (*e.g.*, polyaniline,[5,6] polypyrrole[7,8] and their derivatives) have been widely studied as pseudo-capacitive materials and have shown high gravimetric and volumetric pseudo-capacitance in various non-aqueous electrolytes. When used as bulk materials, conducting polymers generally suffered from a limited cycle stability. Recently, transition metal oxides,[9–12] hydroxides[13,14] and sulfides[15–18] received more attentions owing to their high specific pseudo-capacitance and low-cost, but suffered from the high electrical resistance, resulting in the low power density. At present, nanostructuring redox-active materials to increase pseudo-capacitance and building hybrid systems to achieve high energy density are the two most effective strategies to develop high performance electrode materials for SCs application.

MnO_2 is one of the most promising pseudo-capacitive materials due to its high theoretical capacity of ~1400 F g^{-1}, wide operating potential window, low-cost, natural abundance and environmental compatibility.[19–21] However, the actual value of specific capacitance is deviated far from the theoretical value, which is ascribed to its poor electrical conductivity and slow ion diffusion rate. To overcome this limitation, deposition of

[a]*School of Materials Science and Engineering, Hefei University of Technology, Hefei 230009, China. E-mail: jqliu@hfut.edu.cn*
[b]*School of Chemistry and Chemical Engineering, Hefei University of Technology, Hefei 230009, China*
[c]*Key Laboratory of Advanced Functional Materials and Devices of Anhui Province, Hefei 230009, China*
[d]*Department of Electronic Materials Engineering, Research School of Physics and Engineering, The Australian National University, Canberra, ACT 2601, Australia*

† Electronic supplementary information (ESI) available. See DOI: 10.1039/c7ra04883a

nanostructured pseudo-capacitive MnO_2 onto highly ordered, high-surface-area and high conductivity nano-frameworks (acting as current collectors) such as carbon nanotubes[22,23] and nanofibers,[24,25] graphene,[26,27] and transition metal oxides nanostructures[28–31] *etc.*, has been well demonstrated to be an effective and promising approach.

Highly ordered TiO_2 nanotube arrays (TNTAs) anodized from Ti foils hold great promise as supercapacitor electrode materials owing to their high-surface-area, chemical stability, direct electron transport pathways and simple fabrication. Moreover, TNTAs may serve as a good support for nano-structured high specific capacitance materials to form hybrid systems. However, the poor electric conductivity of TNTAs that derives from the n-type semiconductor nature rendered them not the ideal current collectors for the application of constructing high performance SCs. In our previous work, annealing in H_2-contained atmosphere[32] and carbon layer[33] modification of TiO_2 nanotubes (NTs) have demonstrated electrical conductivity enhancement of dozens of times than that of the pristine TNTAs. Then Nickel oxide,[32] Cu_2O[34] and Co_3O_4 [35] layer were successfully loaded onto both the inner and outer walls of TiO_2 NTs for constructing various TNTAs-based electrodes with high supercapacitive performance.

Herein, a novel-structured MnO_2/EH-TNTAs electrode with superior supercapacitive performance was developed by galvanostatic electrodepositing MnO_2 nanoflakes (NFs) onto both the outer and inner walls of electrochemically hydrogenated TNTAs (EH-TNTAs). The as-fabricated MnO_2/EH-TNTAs electrode yields a specific capacitance of up to 650.0 A g^{-1} at 1.0 A g^{-1} with 86.9% of the initial capacitance remaining after 5000 charge/discharge cycles at 5 A g^{-1}, outperforming the best performance of reported MnO_2–TNTAs hybrids. Now that facile and cost-effective fabrication of high performance MnO_2/EH-TNTAs electrode for SCs application could be achieved *via* a full electrochemical approach. More importantly, impacts of different strategies for TNTAs hydrogenation and MnO_2 depositing on the electrochemical performance of the resulting MnO_2/TNTAs electrodes as well as the corresponding mechanism are also proposed in detail. Our research results will provide theoretical and technical guideline for the application of TNTAs-based electrode in the SCs.

Experimental section

Preparation of TNTAs

Highly ordered and well-separated TNTAs were directly grown on a Ti foil (0.1 mm, 99.7%) using electrochemical anodization. Prior to anodization, Ti foils were ultrasonically cleaned in acetone, ethanol, and deionized water, respectively, for 20 min. Electrochemical anodization was conducted on a two-electrode setup using a DC voltage of 60 V for 6 h in ice bath. A Ti foil was used as the working electrode, a graphite foil as the cathode, a solution of 0.25 M NH_4F in ethylene glycol with 8 vol% H_2O as the electrolyte. After anodization, the as-fabricated amorphous TNTAs were annealed in air at 500 °C for 2 h with a heating rate of 2 °C min^{-1}, and the corresponding sample was named as air-TNTAs.

Electrochemical hydrogenation of TNTAs

Electrochemical hydrogenation of TNTAs to obtain the EH-TNTAs was conducted on a two-electrode setup using a DC voltage of 4 V for 20 min at room temperature. The as-fabricated air-TNTAs sample was used as the cathode, a graphite foil as the anode, and an aqueous solution of 0.1 M Na_2SO_4 as the electrolyte. For comparison, hydrogenation was also conducted by means of annealing the amorphous TNTAs in H_2-contained atmosphere (10% H_2 + 90% Ar), and the corresponding sample was labelled as H_2-TNTAs.

Preparation of MnO_2/EH-TNTAs

A galvanostatic electrodeposition (GED) approach was adopted for the fabrication of MnO_2/EH-TNTAs composites. In a typical synthesis, MnO_2 depositing was performed on a three-electrode system at 0.5 mA cm^{-2} for 120 s with the EH-TNTAs, a Pt wire, and a Ag/AgCl (saturated KCl) electrode as working, counter, and reference electrodes, respectively, using a 0.01 M $MnSO_4$ aqueous solution as electrolyte. Actually, impacts of current density, depositing time as well as the electrolyte concentration on the microstructure, morphology and pseudocapacitive performance of MnO_2/EH-TNTAs were systematically studied in our research work. Owing to space limitation, we will discuss in detail elsewhere. MnO_2/EH-TNTAs electrode discussed in this work was fabricated with optimized parameters. The fabrication process of electrode materials is illustrated in Fig. 1.

For comparison, MnO_2/air-TNTAs and MnO_2/H_2-TNTAs were also prepared by galvanostatic electrodepositing MnO_2 onto the walls of air-TiO_2 NTs and H_2–TiO_2 NTs respectively. Furthermore, MnO_2 was also deposited onto both the bare Ti foil and the walls of EH-TiO_2 NTs using our previously reported chemical bath deposition (CBD) technique,[36] and the resulting samples were labelled as MnO_2/Ti and EH-TNTAs@MnO_2 respectively.

Material characterization

Morphologies were observed using FESEM (SU-8020, operated at 5.0 kV) and TEM (JEM-2100F, operated at 200 kV) equipped with an Oxford INCA energy dispersive X-ray (EDX) analyser. Structural features of as-prepared samples were identified by XRD (Rigaku D/Max-2500 V) and Raman spectroscopy (Lab-RAM HR Evolution). The chemical constituents were investigated by XPS (ESCALAB250Xi). Nitrogen adsorption isotherms were conducted at 77.15 K on a SA3100 Micromeritics analyzer after degassing samples at 373.15 K for 2 h, and the BET surface area was estimated in a relative pressure range from 0.05 to 0.2.

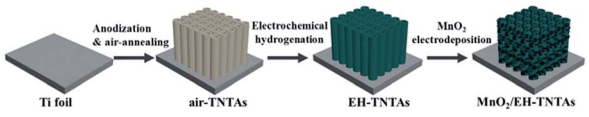

Fig. 1 Schematic illustration for the synthesis of MnO_2/EH-TNTAs electrode.

Electrochemical evaluation

All electrochemical measurements were carried out on an electrochemical workstation (Autolab PGSTAT302N) in a three-electrode system using the tested sample, a Pt wire, an Ag/AgCl (3 M KCl) electrode as the working, counter, and reference electrodes, respectively, and using 0.5 M Na_2SO_4 aqueous solution as electrolyte. The electrochemical properties of the tested samples were investigated by cyclic voltammetry (CV) and galvanostatic charge–discharge (GCD) testing. Electrochemical impedance spectroscopy (EIS) measurements were conducted in the frequency ranging from 10 mHz to 100 kHz at open-circuit potential with a AC-voltage amplitude of 5 mV. The cycling stability of the electrode was evaluated by GCD at 5 A g^{-1} for 5000 cycles.

Results and discussion

Highly ordered and well-separated TiO_2 NTs were fabricated by anodization of Ti foils, and then annealed in air. The as-formed TiO_2 NTs have a uniform diameter of ~180 nm, a wall thickness of ~25 nm (Fig. 2a) and a length of ~10 μm (Fig. S1†). The obvious difference to the conventional TNTAs is that the TiO_2 NTs are free-standing and well-separated from each other with intertube spacings ranging from 8 to 20 nm. The free space among the tubes allows for more exposed outer surface for the deposition of a secondary material as well as efficient mass transport. After electrochemical hydrogenation (EH), the obtained EH-TNTAs display no differences in tubular structure compared to air-TNTAs (Fig. 2b). Worth mentioning here is that the EH-TNTAs evidence a dark blue colour *versus* the grey air-TNTAs, indicating a strong absorption in the visible region due to hydrogen diffusion into TiO_2 lattice during the EH process. All microstructures of EH-TNTAs enable them to serve as a good support for the capacitive active materials to form composite structures. Besides, XRD patterns of both air-TNTAs, and EH-TNTAs show almost the same diffraction patterns (Fig. 2d), and all diffraction peaks could be well indexed to the characteristic peaks of anatase TiO_2 (JCPDS#21-1272) except for the Ti peaks. That means amorphous structure transforms to anatase phase upon thermal treatment, while no phase transformation occurs during the EH process. Then, depositing MnO_2 onto EH-TiO_2 NTs was achieved *via* GED approach (Fig. 2c and S1†). FESEM analysis revealed that both the outer and inner walls of the EH-TiO_2 NTs were fully and uniformly coated with large amounts of tiny NFs. These NFs intersect with each other, thus constructing a 3D porous cotton-like structure. Moreover, the tube-mouths were not blocked by MnO_2 deposit and the intertube spacings remained interconnected. TEM observation further revealed that compare to the smooth surface of EH-TiO_2 NTs, surface of MnO_2/EH-TiO_2 NTs became rough and bumpy due to the full dispersion of tiny MnO_2 NFs (Fig. 3a). In HRTEM image (Fig. 3b), *d* space of 3.50 Å corresponding to the (101) planes of anatase TiO_2 could be observed clearly, while no well-defined lattice fringes for MnO_2 crystal. This demonstrated the high crystallinity for TNTAs but amorphous or low crystallinity for MnO_2. XRD analysis also confirmed the amorphous structure for MnO_2. No identifiable peaks related to MnO_2 crystal emerge in the MnO_2/EH-TNTAs pattern. Energy-dispersive X-ray spectrometry (EDS) mapping analysis for a hybrid single nanotube (Fig. 3c–f) further confirmed the MnO_2/EH-TNTAs hybrid with elements Ti, O, and Mn resulting from TiO_2 NTs and MnO_2 NFs. More dense element distribution of Ti and O than that of Mn indicates the element Mn resulting from MnO_2 fully and uniformly distributed on the surface of EH-TiO_2 NTs.

X-ray photoelectron spectroscopy (XPS) and Raman spectroscopy studies were conducted to reveal the effect of EH process on the chemical composition and oxidation state of TNTAs. Fig. 4a compares the normalized Ti 2p core level XPS spectra of air-TNTAs (black curve) and EH-TNTAs (red curve), together with their difference spectrum. Two peaks centered at 465.33 and 459.13 eV that correspond to the characteristic Ti $2p_{1/2}$ and Ti $2p_{3/2}$ peaks of Ti^{4+} are observed for both samples. In contrast to air-TNTAs, both Ti $2p_{1/2}$ and Ti $2p_{3/2}$ peaks for EH-TNTAs shift to the lower binding energy, suggesting that they

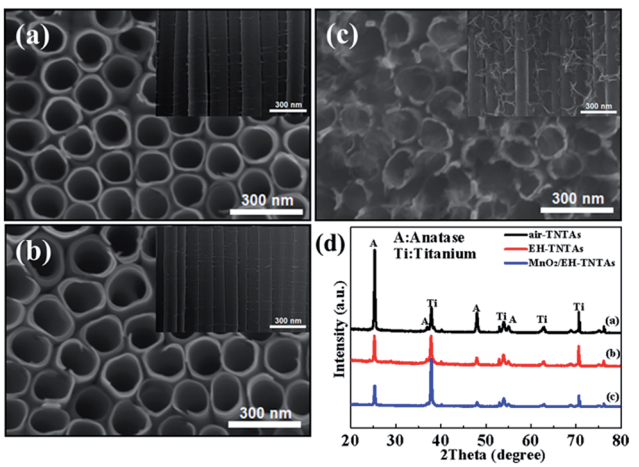

Fig. 2 FESEM images of (a) air-TNTAs, (b) EH-TNTAs, and (c) MnO_2/EH-TNTAs (insets are the corresponding side-view images), (d) XRD patterns of air-TNTAs, EH-TNTAs and MnO_2/EH-TNTAs.

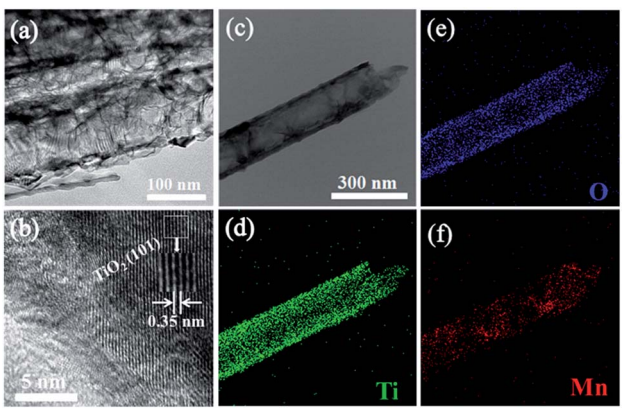

Fig. 3 TEM (a) and HRTEM (b) images of MnO_2/EH-TNTAs, TEM image of one single MnO_2/EH-TiO_2 NT (c) and the corresponding EDS mapping of Ti (d), O (e), Mn (f).

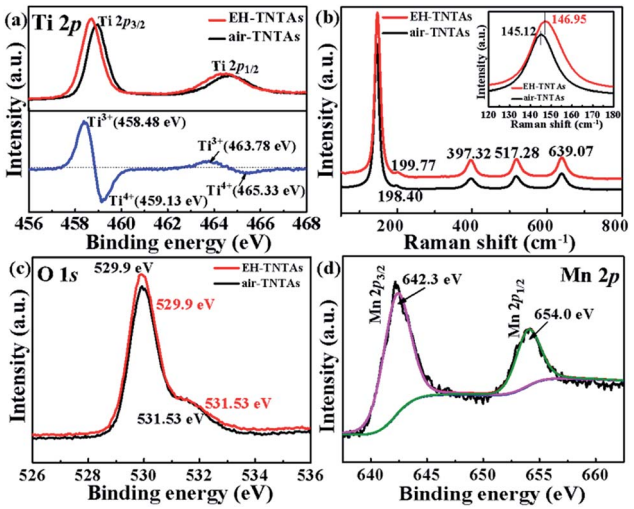

Fig. 4 XPS spectra of (a) Ti 2p, (c) O 1s and (b) Raman spectra of air-TNTAs and EH-TNTAs, (d) XPS spectra of Mn 2p of MnO_2/EH-TNTAs.

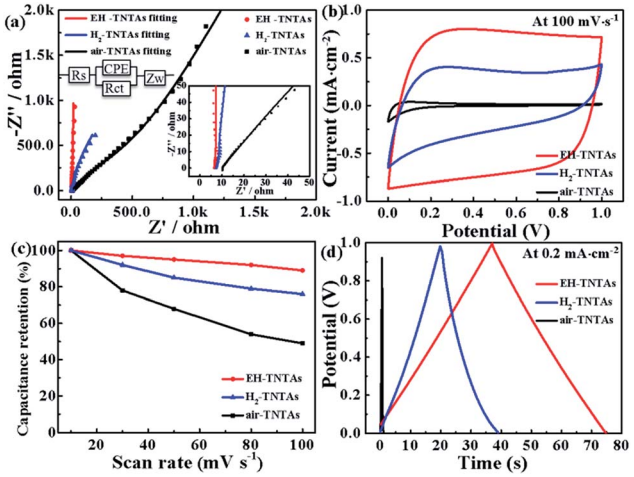

Fig. 5 Nyquist plots (a), CV curves (b), capacitance retention (c), and GCD curves (d) of air-TNTAs, H_2-TNTAs and EH-TNTAs electrodes, two insets in (a) are the magnified view of the high-frequency region and the equivalent circuit for all TNTAs electrodes, respectively.

have different bonding environments. By subtracting the normalized Ti 2p spectra of EH-TNTAs with air-TNTAs, two extra peaks centered at 463.78 and 458.48 eV are clearly observed. These two peaks are attributed to the characteristic Ti $2p_{1/2}$ and Ti $2p_{3/2}$ peaks of Ti^{3+}, proving that Ti^{3+} sites (oxygen vacancies) are created during EH process.[37–39] Same conclusion was also obtained from Raman analysis (Fig. 4b). The characteristic peaks at 145.12 cm^{-1} (E_g), 198.40 cm^{-1} (E_g), 397.32 cm^{-1} (B_{1g}), 517.28 cm^{-1} (A_{1g}/B_{1g}) and 639.07 cm^{-1} (E_g) in the air-TNTAs are assigned to anatase TiO_2. Interestingly, a slightly blue-shift of E_g peaks at 146.95 cm^{-1} and 199.77 cm^{-1} can be identified in EH-TNTAs, suggesting the increased amount of oxygen vacancies that originate from Ti^{4+} reduction.[40–42] Moreover, O 1s XPS spectra of air-TNTAs (black curve) and EH-TNTAs (red curve) are shown in Fig. 4c. The peaks centered at 529.90 and 531.53 eV for both air-TNTAs and EH-TNTAs are attributed to Ti–O and surface Ti–OH groups.[40,43,44] There is no noticeable difference in the peak at 531.53 eV between air-TNTAs and EH-TNTAs, implying that the hydrogenation process does not change the surface species of EH-TNTAs. Mn 2p XPS spectra of MnO_2/EH-TNTAs reveals two peaks located at 642.3 and 654.0 eV (Fig. 4d), which are consistent with the characteristic Mn $2p_{3/2}$ and Mn $2p_{1/2}$ binding energies of MnO_2 and confirm the successful MnO_2 deposition.[25,39,45]

To evaluate the electrical properties of various TNTAs electrodes, EIS measurements were subsequently performed at open circuit potential with an amplitude of 5 mV. Fig. 5a shows the Nyquist plots of the air-TNTAs, H_2-TNTAs and EH-TNTAs electrodes. It is obvious that EH-TNTAs electrode shows much lower impedance value than both air-TNTAs and H_2-TNTAs electrodes. Moreover, note that the plot of EH-TNTAs exhibits an even steeper impedance line (nearly vertical) in comparison to H_2-TNTAs, which demonstrates the superior capacitive performance for EH-TNTAs electrode. For quantitative analysis, experimental data of impedance spectra were fitted to the model depicted by the equivalent circuit (inset in Fig. 5a). In this model, R_s is the solution resistance, R_{ct} represents the inherent resistance of the working electrode together with the charge transfer resistance through the electrolyte, the constant phase element (CPE) refers to the double layer capacitance, and Z_w is the Warburg impedance. Table S1† lists the fitted parameter values for various TNTAs electrodes. The R_{ct} for air-TNTAs is up to 1475.0 Ω, while only 279.20 and 22.38 Ω for H_2-TNTAs and EH-TNTAs respectively, and the EH-TNTAs electrode has the lowest R_{ct}. This dramatic decline in the resistance of EH-TNTAs electrode can be attributed to the greatly improved conductivity of the electrode and efficient charge carrier transport induced by the introduction of large numbers of oxygen vacancies during the EH process.

Besides, in order to investigate the effect of EH process on the electrochemical properties of various TNTAs electrodes, CV curves were first collected (from 10 to 100 mV s^{-1}, Fig. S2†). In comparison to air-TNTAs and H_2-TNTAs, EH-TNTAs electrode exhibits the best capacitive performance by delivering CV profiles with higher current density and closer to ideal rectangular shape (Fig. 5b). Areal capacitance of the electrodes as a function of scan rate were calculated and shown in Table S2.† EH-TNTAs achieves an areal capacitance up to 6.96 mF cm^{-2} at 100 mV s^{-1}, which is significantly higher than that of air-TNTAs (0.18 mF cm^{-2}) and H_2-TNTAs (3.14 mF cm^{-2}). The capacitance retentions of EH-TNTAs at different scan rates are obviously higher than that of air-TNTAs and H_2-TNTAs, revealing the good rate capability (Fig. 5c). The rate capability is related to the ion diffusion rate and conductivity of the electrode. Given that the morphologies of all TNTAs electrodes are similar, they should have similar ion diffusion rate. Therefore, the improved rate capacitance in EH-TNTAs should be due to the greatly enhanced electrical conductivity. The corresponding GCD curves of different TNTAs electrodes were also collected at different current densities (Fig. S3†). Obviously that GCD curves of EH-TNTAs electrode are symmetric and substantially prolonged over the air-TNTAs and H_2-TNTAs electrodes, also revealing

good capacitive behavior for EH-TNTAs. Fig. 5d compares the GCD curves of these TNTAs electrodes at 0.2 mA cm^{-2}. The areal capacitance of EH-TNTAs is calculated to be 7.5 mF cm^{-2}, which is also substantially higher than the values obtained from the air-TNTAs (0.1 mF cm^{-2}) and H_2-TNTAs (3.8 mF cm^{-2}). Therefore, above electrochemical analysis demonstrated that greatly enhanced electrical properties and electrochemical performance enabled EH-TNTAs to serve as an ideal current collector for the application of constructing high performance SCs.

MnO_2, as one of the most promising pseudocapacitive materials with high theoretical specific capacitance was successfully loaded onto EH-TiO_2 NTs using GED technique. SEM and TEM analysis show that both outer and inner surfaces of EH-TiO_2 NTs are fully and uniformly coated with MnO_2 NFs. In order to gain deeper insight regarding the effectiveness of TiO_2 support, CV curves of different MnO_2/TNTAs electrodes as well as MnO_2/Ti electrode were firstly collected from 10 to 100 mV s^{-1}, as shown in Fig. S4.† The specific capacitance were calculated and listed in Table. S3.† Obviously, the capacitances of all MnO_2/TNTAs electrodes are substantially higher than the MnO_2/Ti electrode, suggesting the tubular TiO_2 substrate has a progressive and positive effect on the capacitive behavior of the deposited MnO_2 compared to the planar Ti substrate. Futher, CV curves of different MnO_2/TNTAs electrodes exhibit rectangular-like shape and good symmetry at various scan rates, revealing good capacitive behaviour. Significantly, MnO_2/EH-TNTAs exhibit greatly enhanced capacitive current density compare to both MnO_2/air-TNTAs and MnO_2/H_2-TNTAs (Fig. 6a). The specific capacitance of MnO_2/EH-TNTAs achieves 558.9 F g^{-1} at 10 mV s^{-1} based on the MnO_2 mass, which is approximately 1.7 and 2.5 times that of MnO_2/H_2-TNTAs (326.4 F g^{-1}) and MnO_2/air-TNTAs (218.8 F g^{-1}). Furthermore, MnO_2/EH-TNTAs electrode shows good rate capability with a capacitance retention of 63.52% when the scan rate increase from 10 to 100 mV s^{-1}, while it is only 31.9% and 48.1% for MnO_2/air-TNTAs and MnO_2/H_2-TNTAs respectively. The corresponding GCD tests were also operated at different current densities (from 1 A g^{-1} to 10 A g^{-1}, Fig. S5†). GCD curves of different MnO_2/TNTAs electrodes are symmetric with nearly linear slopes, indicating the high-rate capability and good reversibility. The specific capacitance of MnO_2/EH-TNTAs reaches up to 650 F g^{-1} at 1 A g^{-1}, which is substantially larger than the values obtained from MnO_2/H_2-TNTAs (388.7 F g^{-1}), MnO_2/air-TNTAs (290.7 F g^{-1}) and MnO_2/Ti (257.7 F g^{-1}) electrodes (Fig. 6b and Table S3†). Thus, both GCD and CV results suggest that the electrochemical performance of MnO_2/TNTAs composites is strongly correlated to TiO_2 support. Compare to the air-TNTAs, H_2-TNTAs or various reported supports for MnO_2 deposition summarized in Table S4,† EH-TNTAs with superior electrical conductivity and efficient charge separation and transport was proved to be an excellent support for electrochemically active MnO_2.

How the MnO_2 depositing technique affecting the electrochemical performance of MnO_2/TNTAs composites was further explored. Compare to our reported[36] EH-TNTAs@MnO_2 fabricated by CBD approach, MnO_2/EH-TNTAs exhibits much higher electrochemical performance, as shown in Fig. 7. The specific capacitance of MnO_2/EH-TNTAs reaches up to 650 F g^{-1}, much larger than that of EH-TNTAs@MnO_2 (523.90 F g^{-1}) at the same current density of 1 A g^{-1}. Since both adopted the EH-TNTAs as the support, the enhanced electrochemical performance of MnO_2/EH-TNTAs should be ascribed to MnO_2 deposit.

Lot of studies reported that how to maximize the electrochemically active sites for redox reactions is the key point to achieve high energy storage density of MnO_2. Increasing specific surface area and obtaining 3D porous structures are the two most effective strategies. Microstructure characteristics of MnO_2 deposited by two different techniques were firstly compared, as shown in Fig. S6.† Obviously that ultrafine MnO_2 NFs in EH-TNTAs@MnO_2 obtained by CBD technique are densely-packed together to form a thin layer, while MnO_2 NFs in MnO_2/EH-TNTAs achieved by GED technique intersect with each other, thus constructing a 3D porous cotton-like structure.

As is known to all, materials with a 3D porous structure are beneficial for reducing the ion diffusion resistance and optimizing the transport kinetics, which could ensure that porous MnO_2 possesses both high energy density and power capability. Moreover, 3D porous structure should render the material a higher specific area, accordingly the relative BET surface area of the testing samples was measured and calculated *via* a special self-defined method (Table S5†). As expected that 3D porous structured MnO_2 enabled the MnO_2/EH-TNTAs the higher relative BET specific area compared to EH-TNTAs@MnO_2 with densely-packed MnO_2. Consequently MnO_2/EH-TNTAs with larger surface area is capable to provide more electrochemically active sites to electrolyte for a fast surface redox reaction, which contributes to the high pseudocapacitance and good rate capability.[21,46,47] CV curves of the MnO_2/EH-TNTAs electrode show no

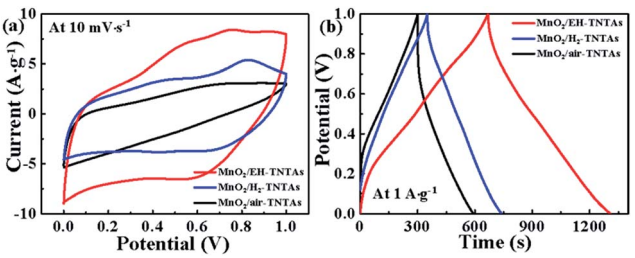

Fig. 6 (a) CV curves at 10 mV s^{-1}, and (b) CD curves at 1 A g^{-1} of the MnO_2/air-TNTAs, MnO_2/H_2-TNTAs and MnO_2/EH-TNTAs electrodes.

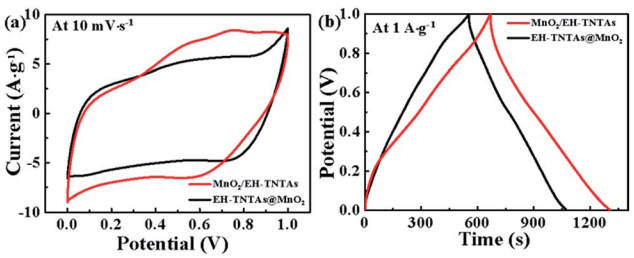

Fig. 7 (a) CV curves at 10 mV s^{-1}, and (b) GCD curves at 1 A g^{-1} of the MnO_2/EH-TNTAs and EH-TNTAs@MnO_2 electrodes.

obvious distortion from 10 to 100 mV s^{-1}, proving the excellent ion diffusion in the electrode. Therefore, the unique 3D porous cotton-like structure of MnO_2 and larger specific surface area endowed the MnO_2/EH-TNTAs electrode with superior supercapacitive performance.

More importantly, the MnO_2/EH-TNTAs electrode displays promising cyclability. As shown in Fig. S7,† MnO_2/EH-TNTAs retains 86.9% of its original capacitance after 5000 cycles at 5 A g^{-1}, indicating the excellent stability of the deposited 3D porous MnO_2 during the charge–discharge process, which is favourable for practical applications.

Conclusions

In summary, electrochemically hydrogenation significantly improves the electrical conductivity and electrochemical capacitance of TNTAs. The as-fabricated EH-TNTAs were proved to be an efficient current collector as well as an outstanding support for constructing high-performance supercapacitor electrode materials with nano-structured high specific capacitance materials. Further, depositing MnO_2 NFs onto both the outer and inner walls of EH-TiO_2 NTs was successfully achieved *via* a facile GED technique. The MnO_2/EH-TNTAs electrode delivers a specific capacitance of up to 650.0 F g^{-1} at 1.0 A g^{-1} with 86.9% of the initial capacitance remaining after 5000 charge/discharge cycles at 5 A g^{-1}, outstripping other reported MnO_2–TNTAs electrodes. Comprehensive characterization and electrochemical analysis demonstrate that the superior supercapacitive performance of MnO_2/EH-TNTAs electrode mainly results from the synergistic effect of unique 3D cotton-like porous structure and high specific surface area of MnO_2 as well as remarkably improved electrical conductivity and electrochemical performances of EH-TNTAs.

Acknowledgements

This work was financially supported by the National Natural Science Foundation of China (51402078, 51302060), the National Basic Research Program of China (973 Program, 2014CB660815), and Young Scholar Enhancement Foundation (Plan B) of Hefei University of Technology (JZ2016HGTB0711, JZ2016HGTB0719).

Notes and references

1 Y. Wang, Y. Song and Y. Xia, *Chem. Soc. Rev.*, 2016, **45**, 5925–5950.
2 B. C. Kim, J.-Y. Hong, G. G. Wallace and H. S. Park, *Adv. Energy Mater.*, 2015, **1500959**, 1–33.
3 C. Yuan, H. B. Wu, Y. Xie and X. W. Lou, *Angew. Chem., Int. Ed. Engl.*, 2013, **53**, 1488–1504.
4 M.-M. Titirici, R. J. White, N. Brun, V. L. Budarin, D. S. Su, F. d. Monte, J. H. Clarkd and M. MacLachlan, *Chem. Soc. Rev.*, 2014, **44**, 250–290.
5 Z. Shao, H. Li, M. Li, C. Li, C. Qu and B. Yang, *Energy*, 2015, **87**, 578–585.
6 Y. Zhao, Z. Zhang, Y. Ren, W. Ran, X. Chen, J. Wu and F. Gao, *J. Power Sources*, 2015, **286**, 1–9.
7 J. S. Lee, D. H. Shin and J. Jang, *Energy Environ. Sci.*, 2015, **8**, 3030–3039.
8 Z. H. Huang, Y. Song, X. X. Xu and X. X. Liu, *ACS Appl. Mater. Interfaces*, 2015, **7**, 25506–25513.
9 Q. Cheng, J. Tang, J. Ma, H. Zhang, N. Shinya and L.-C. Qin, *Carbon*, 2011, **49**, 2917–2925.
10 Z. Peng, X. Liu, H. Meng, Z. Li, B. Li, Z. Liu and S. Liu, *ACS Appl. Mater. Interfaces*, 2016, **9**, 4577–4586.
11 V. Kannan, A. I. Inamdar, S. M. Pawar, H.-S. Kim, H.-C. Park, H. Kim, H. Im and Y. S. Chae, *ACS Appl. Mater. Interfaces*, 2016, **8**, 17220–17225.
12 A. García-Gómez, S. Eugénio, R. G. Duarte, T. M. Silva, M. J. Carmezim and M. F. Montemor, *Appl. Surf. Sci.*, 2016, **382**, 34–40.
13 X. Xiong, D. Ding, D. Chen, G. Waller, Y. Bu, Z. Wang and M. Liu, *Nano Energy*, 2015, **11**, 154–161.
14 J. Xing, S. Wu and K. Y. S. Ng, *RSC Adv.*, 2015, **5**, 88780–88786.
15 X. Xiong, G. Waller, D. Ding, D. Chen, B. Rainwater, B. Zhao, Z. Wang and M. Liu, *Nano Energy*, 2015, **16**, 71–80.
16 X. Ou, X. Xiong, F. Zheng, C. Yang, Z. Lin, R. Hu, C. Jin, Y. Chen and M. Liu, *J. Power Sources*, 2016, **325**, 410–416.
17 A. M. Patil, V. C. Lokhande, A. C. Lokhande, N. R. Chodankar, T. Ji, J. H. Kim and C. D. Lokhande, *RSC Adv.*, 2016, **6**, 68388–68401.
18 X. Xiong, G. Wang, Y. Lin, Y. Wang, X. Ou, F. Zheng, C. Yang, J.-H. Wang and M. Liu, *ACS Nano*, 2016, **10**, 10953–10959.
19 J.-G. Wang, F. Kang and B. Wei, *Prog. Mater. Sci.*, 2015, **74**, 51–124.
20 L. Zhao, J. Yu, W. Li, S. Wang, C. Dai, J. Wu, X. Bai and C. Zhi, *Nano Energy*, 2014, **4**, 39–48.
21 W. Wei, X. Cui, W. Chen and D. G. Ivey, *Chem. Soc. Rev.*, 2011, **40**, 1697–1721.
22 H. Huang, W. Zhang, Y. Fu and X. Wang, *Electrochim. Acta*, 2015, **152**, 480–488.
23 D. Z. W. Tan, H. Cheng, S. T. Nguyen and H. M. Duong, *Mater. Technol.*, 2014, **29**, A107–A113.
24 F. Miao, C. Shao, X. Li, N. Lu, K. Wang, X. Zhang and Y. Liu, *Energy*, 2016, **95**, 233–241.
25 D. Zhou, H. Lin, F. Zhang, H. Niu, L. Cui, Q. Wang and F. Qu, *Electrochim. Acta*, 2015, **161**, 427–435.
26 L. Peng, X. Peng, B. Liu, C. Wu, Y. Xie and G. Yu, *Nano Lett.*, 2013, **13**, 2151–2157.
27 Y. He, W. Chen, X. Li, Z. Zhang, J. Fu, C. Zhao and E. Xie, *ACS Nano*, 2013, **7**, 174–182.
28 X. Lu, M. Yu, G. Wang, T. Zhai, S. Xie, Y. Ling, Y. Tong and Y. Li, *Adv. Mater.*, 2013, **25**, 267–272.
29 Z. Ma, G. Shao, Y. Fan, M. Feng, D. Shen and H. Wang, *ACS Sustainable Chem. Eng.*, 2017, **5**, 4856–4868.
30 Z. Ma, G. Shao, Y. Fan, G. Wang, J. Song and D. Shen, *ACS Appl. Mater. Interfaces*, 2016, **8**, 9050–9058.
31 X. Xia, D. Chao, Z. Fan, C. Guan, X. Cao, H. Zhang and H. J. Fan, *Nano Lett.*, 2014, **14**, 1651–1658.

32 L. H. Cui, Y. Wang, X. Shu, J. F. Zhang, C. P. Yu, J. W. Cui, H. M. Zheng, Y. Zhang and Y. C. Wu, *RSC Adv.*, 2016, **6**, 12185–12192.
33 C. Yu, Y. Wang, J. Zhang, X. Shu, J. Cui, Y. Qin, H. Zheng, J. Liu, Y. Zhang and Y. Wu, *New J. Chem.*, 2016, **40**, 6881–6889.
34 Y. Qin, J. Zhang, Y. Wang, X. Shu, C. Yu, J. Cui, H. Zheng, Y. Zhang and Y. Wu, *RSC Adv.*, 2016, **6**, 47669–47675.
35 C. Yu, Y. Wang, H. Zheng, J. Zhang, W. Yang, X. Shu, Y. Qin, J. Cui, Y. Zhang and Y. Wu, *J. Solid State Electrochem.*, 2017, **21**, 1069–1078.
36 X. Juan, L. Jia-Qin, L. Jing-Wei, W. Yan, L. Jun and W. Yu-Cheng, *Acta Phys.-Chim. Sin.*, 2016, **32**, 2545–2554.
37 X. Lu, G. Wang, T. Zhai, M. Yu, J. Gan, Y. Tong and Y. Li, *Nano Lett.*, 2012, **12**, 1690–1696.
38 H. Zhou and Y. Zhang, *J. Power Sources*, 2013, **239**, 128–131.
39 Z. Pei, M. Zhu, Y. Huang, Y. Huang, Q. Xue, H. Geng and C. Zhi, *Nano Energy*, 2016, **20**, 254–263.
40 H. Wu, D. Li, X. Zhu, C. Yang, D. Liu, X. Chen, Y. Song and L. Lu, *Electrochim. Acta*, 2014, **116**, 129–136.
41 H. Cui, W. Zhao, C. Yang, H. Yin, T. Lin, Y. Shan, Y. Xie, H. Gu and F. Huang, *J. Mater. Chem. A*, 2014, **2**, 8612–8616.
42 J. Huo, Y. Hu, H. Jiang and C. Li, *Nanoscale*, 2014, **6**, 9078–9084.
43 Z. Li, Y. Ding, W. Kang, C. Li, D. Lin, X. Wang, Z. Chen, M. Wu and D. Pan, *Electrochim. Acta*, 2014, **161**, 40–47.
44 J. Zhang, Y. Wang, J. Wu, X. Shu, C. Yu, J. Cui, Y. Qin, Y. Zhang, P. M. Ajayan and Y. Wu, *Chem. Eng. J.*, 2017, **313**, 1071–1081.
45 H. Zhou and Y. Zhang, *J. Power Sources*, 2014, **272**, 866–879.
46 P. Trogadas, V. Ramani, P. Strasser, T. F. Fuller and M.-O. Coppens, *Angew. Chem., Int. Ed.*, 2016, **55**, 122–148.
47 P. Simon and Y. Gogotsi, *Nat. Mater.*, 2008, **7**, 845–854.